BEILSTEIN JOURNAL OF NANOTECHNOLOGY

Influence of an external electric field on the catalytic CO oxidation of nanoscaled CeO_2 and its La^{3+} and Gd^{3+} congeners

Parastoo Jamshidi, Silvio Heinschke and Jörg J. Schneider*§

Full Research Paper

Open Access

Address:
Eduard-Zintl-Institut für Anorganische und Physikalische Chemie, Technische Universität Darmstadt, Peter-Grünberg-Str. 12, Darmstadt, Germany

Email:
Jörg J. Schneider* - joerg.schneider@tu-darmstadt.de

* Corresponding author
§ Phone: +49 (0)6151 1621100, Fax: +49 (0)6151 1621102

Keywords:
cerium oxide; CO oxidation; defect structure; doped cerium oxide; electric potential

Beilstein J. Nanotechnol. **2026,** *17,* 1028–1038.
https://doi.org/10.3762/bjnano.17.70

Received: 10 March 2026
Accepted: 16 July 2026
Published: 04 August 2026

Associate Editor: C. T. Yavuz

Abstract

Herein, we investigate how aliovalent doping and application of an external electrical field modulates the catalytic activity of nanoscale ceria ($n$$CeO_2$) towards CO oxidation. Gd^{3+} and La^{3+} were doped into the $n$$CeO_2$ lattice. Such doping influences the concentration and mobility of oxygen vacancies, which are promoting CO oxidation to CO_2. When applying an electric potential, charge transport within $n$$CeO_2$ is modulated. Our results show that both dopants Gd^{3+} and La^{3+} lead to an increasing V_O concentration, whereas the impact of the applied potential on the oxidation behaviour varies with catalyst composition. The applied electric potential markedly improves the activity of undoped $n$$CeO_2$ and 5% Gd^{3+}-doped $n$$CeO_2$; however, it causes no significant change in CO oxidation capability in 2.5% Gd^{3+}-doped and La^{3+}-doped samples. These findings can be understood considering the applied potential and its influence on the polaron mobility and V_O arrangement, which are controlled by the underlying oxidic defect structure.

Introduction

Catalytic CO oxidation is a straightforward approach to reduce CO levels. A variety of catalysts have been synthesized and applied to improve the efficiency of CO oxidation [1]. The potential applicability of CeO_2 in this reaction as well as in photocatalysis, gas sensing, solar cells, electrocatalysis, and as ultraviolet absorbent has been investigated extensively [2]. CeO_2 crystallizes in the fluorite crystal structure in which each Ce^{4+} is coordinated by eight oxygen anions in a face-centered cubic (fcc) lattice [3]. Characteristically, ceria often shows a mixed valence situation in which both Ce^{4+} and Ce^{3+} exist [4]. Although there are numerous works that have used this mixed valence situation in CeO_2 to influence catalytic properties, current studies still lack investigations of an external electric field to enhance CO oxidation in nanoscaled CeO_2 ($n$$CeO_2$) in the

absence of any precious metals. An external electric field can modify a material's crystal structure and lattice parameters; for example, it drives charge and mass separation and transport and influences heat transfer occurring in the bulk and at surfaces of dielectrics, piezoelectrics, and electrostrictive materials [5-10]. The electric-field-assisted catalytic decomposition over Pt/CeO_2 enables the conversion of methanethiol to H_2S even at low temperatures. An external electric field enhances the formation rates of CH_4 and H_2S [11]. Applying a +10 V potential to Au and Pd nanocatalysts increases the CO oxidation rate by 28% and 14%, respectively [12,13]. Under positive bias, Pt (18–54%) and Pd (14–42%) exhibited markedly higher activity than under negative bias (Pt: 4–8% and Pd: 4–12%) [14,15]. The catalytic decomposition of ammonia over organoboron nanoparticles was also examined under an external electric potential. Applying positive or negative potential allowed the decomposition rate to be tuned between +26% and −37% relative to the zero-bias condition [16], indicating that the sign of the applied potential also affects the overall reaction rate. Very recently, the influence of an electric field on the oxidation of 1,2-dichloroethane on CeO_2 and doped WO_x/CeO_2 has proven that a coupled mechanism of electronic conduction and lattice oxygen migration can be accelerated applying an external electrical field [17].

The oxygen deficiency of CeO_2 can be manipulated in a controlled manner by changing temperature and reduction conditions. Also elemental doping of the underlying fcc solid-state structure may create nonstoichiometric species, for example, $Ce_{1-x}M_xO_{2-\delta}$ (M = metal) [3,16]. Under these conditions oxygen vacancies (V_O) are formed. The incorporated dopant elements thus allow one to modify the coordination environment in the CeO_2 lattice by creating oxygen vacancies, decreasing the energy of V_O formation, and improving charge migration [18-20]. When an V_O is created in doped ceria, one of the unpaired electrons from the vacant oxygen site fills the hole left behind, and the remaining second electron reduces a tetravalent cerium atom. This contrasts with the V_O formation in the undoped ceria surface where two Ce^{4+} atoms are reduced. Doping ceria with various cations influences this general mechanism and changes the energy of the defects and their accessibility, as well as migration energy and migration pathways of mobile ions within the structure [18,21]. With respect to gas adsorption on the surface of ceria this situation is crucial and should vary between undoped and doped $n CeO_2$.

For the first time, we report herein on catalytic studies of CO oxidation on $n CeO_2$ and doped-$n CeO_2$ under an external low-power electric DC potential. Our results show that Gd^{3+}- and La^{3+}-doped $n CeO_2$ influence CO oxidation significantly, but these dopants behave differently when coupling with such low-power electrical fields. In situ FTIR studies were used to follow and monitor the influence of the electrical field by measuring the change in the final gas composition over the headspace of the sample, giving substantial information about the CO oxidation capability on solid $n CeO_2$ under an external electric field.

Results and Discussion

Characterization

A series of $n CeO_2$, containing Gd^{3+} and La^{3+} (2.5% and 5%), was synthesized by a precipitation method (see Supporting Information File 1). XRD patterns are in accord with JCPDS of 34-0394 and prove the fcc structure (Supporting Information File 1, Figures S5–S9) [22]. To investigate the effect of Gd^{3+} and La^{3+} on the doped $n CeO_2$, full width at half maximum (β), the values of interplanar spacing (d), crystallite size (D, Scherrer value), dislocation density (δ value), and number of particles per unit surface area (N value) were calculated based on three different measurements; these values are summarized in Tables S3–S5 (Supporting Information File 1). According to the values of δ and ε, doping of Gd^{3+} and La^{3+} causes a higher defect density in the fcc lattice of $n CeO_2$ as compared to the undoped $n CeO_2$. The structural integrity of the materials after the CO oxidation process was proven spectroscopically (Supporting Information File 1, Figures S10–S14).

In Raman spectra, the characteristic peak corresponding to the F_{2g} mode at ≈470 cm^{-1} is indicative of the symmetry of the lattice (O_h, Supporting Information File 1, Figures S15–S19). The fcc structure is thus confirmed again for all materials. No signals for other phases or impurities are observed [23]. The characteristic peaks related to defects, extrinsic V_O, and intrinsic V_O, appeared around 250, 540, and 600 cm^{-1}, respectively [23,24]. The ceria structure remains stable after the oxidation reaction depicting all characteristic Raman modes; however, additional peaks are observed at wavenumbers higher than 1000 cm^{-1}, indicative either of physisorption or chemisorption of gas molecules on the catalyst surface (Supporting Information File 1, Figures S20–S24).

All cerium oxide nanoparticles are strongly aggregated and form dense strongly corrugated films with an agglomerated particle size of about 50 nm in scanning electron microscopy (SEM) (Supporting Information File 1, Figure S25). Transmission electron microscopy (TEM) and high-resolution transmission electron microscopy (HRTEM) reveal highly crystalline spherical, slightly faceted $n CeO_2$ and 5% doped-$n CeO_2$ with a diameter of around 15 nm (Figure 1a–c). The observed d-spacings are characteristic of $n CeO_2$ (0.31 nm), Gd^{3+}–$n CeO_2$ (0.31 nm), and La^{3+}–$n CeO_2$ (0.29 nm) (Figure 1d–f). This is in accord with the selected-area electron diffraction (SAED) patterns in which pronounced Debye–Scherrer diffraction rings

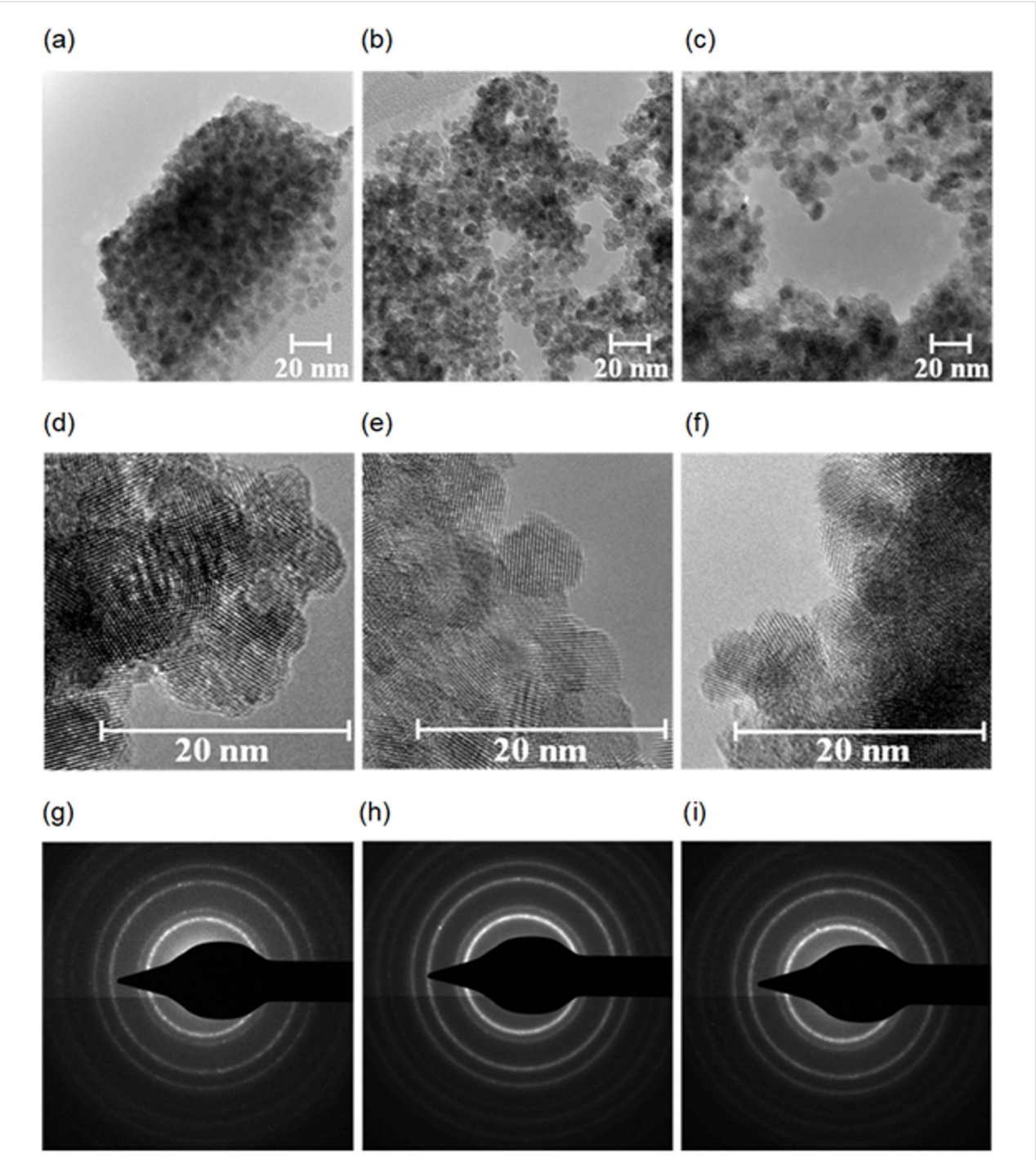

Figure 1: TEM images of (a) nCeO$_2$, (b) 5%Gd^{3+}–nCeO$_2$ and (c) 5%La^{3+}–nCeO$_2$, HRTEM images of (d) nCeO$_2$, (e) 5%Gd^{3+}–nCeO$_2$ and (f) 5%La^{3+}–nCeO$_2$, SAED analysis of (g) nCeO$_2$, (h) 5%Gd^{3+}–nCeO$_2$ and (i) 5%La^{3+}–nCeO$_2$.

can be assigned to (111), (200), (220), and (311) reflections of cubic CeO_2 (Figure 1g–i).

The Brunauer–Emmett–Teller theory (BET) surface areas of the samples are determined in the range from 134 to 148 $m^2 \cdot g^{-1}$ (Supporting Information File 1, Table S6).

CO oxidation on nCeO$_2$ and doped nCeO$_2$ without and with applied electrical field

Figure 2 illustrates CO consumption (I_{CO}) and CO_2 production (I_{CO_2}) for undoped and doped nCeO$_2$ catalysts under field-free conditions with an applied potential of 50 V after 30, 60, 90, and 120 min. The increasing circle size indicates the progres-

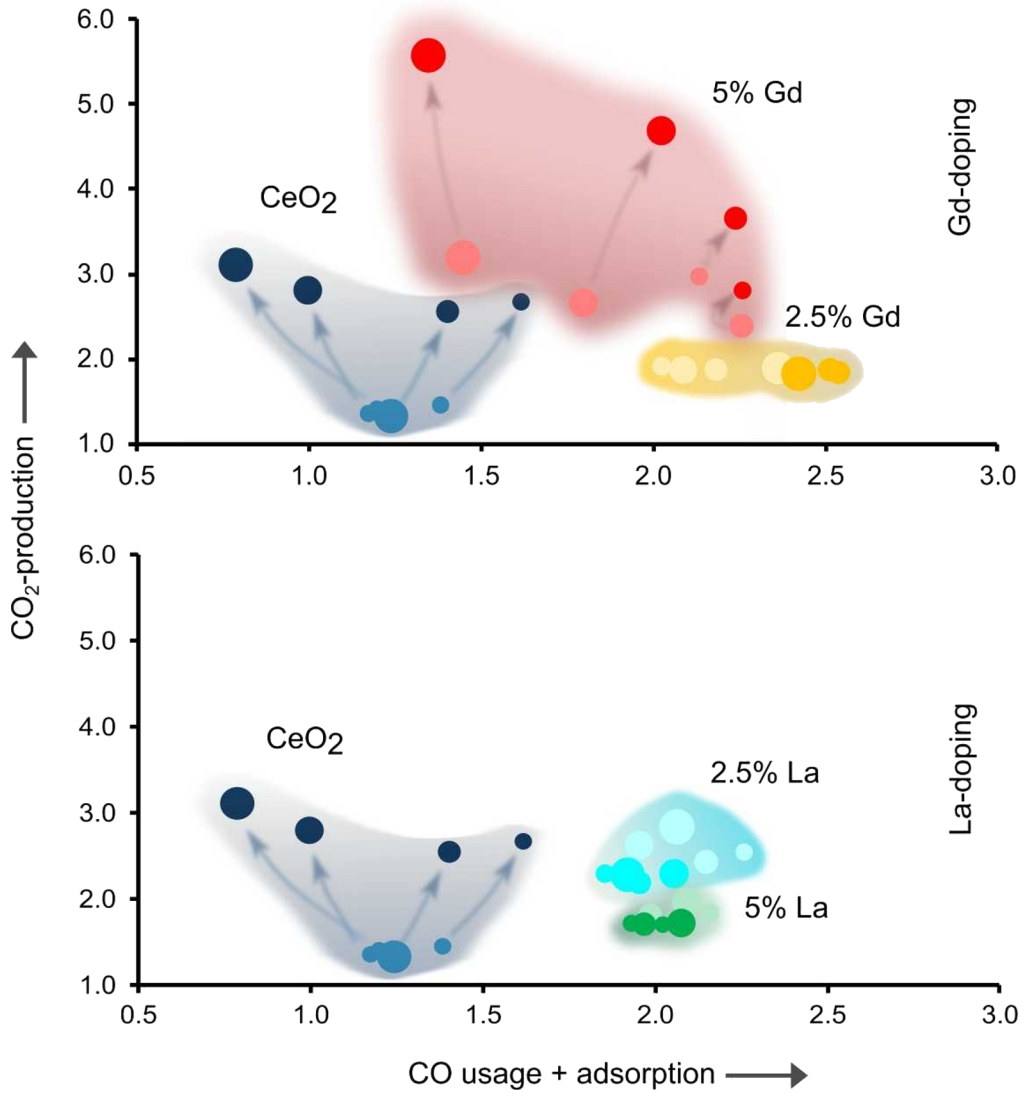

Figure 2: Graphical presentation of the effect of an applied potential (50 V) on CO consumption (I_{CO}) and CO_2 production (I_{CO_2}) over time (30–120 min) for nCeO$_2$ and differently doped nCeO$_2$ catalysts. The arrows indicate the direction of significant changes upon applying potential (50 V). The increasing circle size indicates the progression of reaction time from 30 to 120 min.

sion of reaction time from 30 to 120 min. The arrows indicate the direction of change in I_{CO} and I_{CO_2} values upon application of the electric field. I_{CO} attributes to the CO to CO_2 conversion and to CO adsorption on the sample (light circles). nCeO$_2$ showed I_{CO} of 1.40 g^{-1} and the doping process increased the value up to 2.00 g^{-1}. I_{CO} shows a plateau after 60 min from the beginning of the reaction for all different catalysts, under applied potential conditions as well as without electric potential.

Although applying electric potential (50 V) onto nCeO$_2$ and 5%Gd^{3+}–nCeO$_2$ caused no significant change in I_{CO}, I_{CO_2} increased substantially (Figure 2 top panel). After 120 min, I_{CO_2} increased from 1.32 to 3.11 g^{-1} for nCeO$_2$ and from 3.19 to 5.57 g^{-1} for 5%Gd^{3+}–nCeO$_2$, clearly indicating that the electric field promotes CO oxidation, particularly for 5%Gd^{3+}–nCeO$_2$. It thus reveals an increase for CO_2 production of 170% compared to field-free oxidation conditions. For 2.5%Gd^{3+}–nCeO$_2$, a higher CO uptake was again observed under 50 V; however, CO_2 production remained approximately constant (I_{CO_2} varied from 1.72 to 1.92 g^{-1}) (Figure 2 lower panel). Interestingly and in contrast to the Gd^{3+}-doped samples, applying the same electric potential affects the La^{3+}-doped nCeO$_2$ samples unexpectedly differently. There was no change in I_{CO} under the same electric field for the La^{3+}-doped samples (2.5%La^{3+}–nCeO$_2$: from 2.26 to 2.05 g^{-1} and 5%La^{3+}–nCeO$_2$: from 2.15 to 2.07 g^{-1}). La^{3+}-doped samples showed only small changes in CO_2 production under field-free and under applied-field condi-

tions. I_{CO_2} of 2.5%La^{3+}–$nCeO_2$ and 5%La^{3+}–$nCeO_2$ varied from 2.84 g^{-1} to 2.30, 1.97, and 1.72 g^{-1} under field-free vs applied-field conditions, respectively (Figure 2 lower panel and Supporting Information File 1, Tables S7–S12 and Figures S26–S29).

Without applying potential, trivalent rare-earth doping with La^{3+} and Gd^{3+} increases the V_O concentration and is expected to increase the population of reduced defect states associated with charge compensation [25,26]. Consistent with this, the doped samples show higher CO_2 production than undoped $nCeO_2$ (Figure 3).

External electrical bias has been reported to influence catalytic reactions on solid surfaces by modifying interfacial charge distribution and coupled electronic and ionic defect processes, particularly near surfaces and electrode/oxide interfaces [16,27-30]. In ceria, these processes are closely connected to the Ce^{4+}/Ce^{3+} redox couple and V_O defect chemistry. A small polaron in $nCeO_2$ can be described as a localized electron associated with a Ce^{3+} 4f state, and electronic charge transport is commonly discussed in terms of small-polaron hopping between neighbouring cerium sites (Figure 4, left panel) [31-34]. In parallel, oxygen vacancies may rearrange within the fcc ceria lattice under suitable conditions (Figure 4, middle panel) [35]. In the present work, these processes are used as a phenomenological framework to interpret the observed bias-dependent CO oxidation response (Figure 4, right panel).

A pronounced synergistic enhancement was also observed for 5%Gd^{3+}–$nCeO_2$, whereas the La^{3+}-doped $nCeO_2$ sample showed no measurable bias-induced improvement in catalytic activity. This dopant-dependent response can be rationalized in terms of the different lattice strain and defect interactions

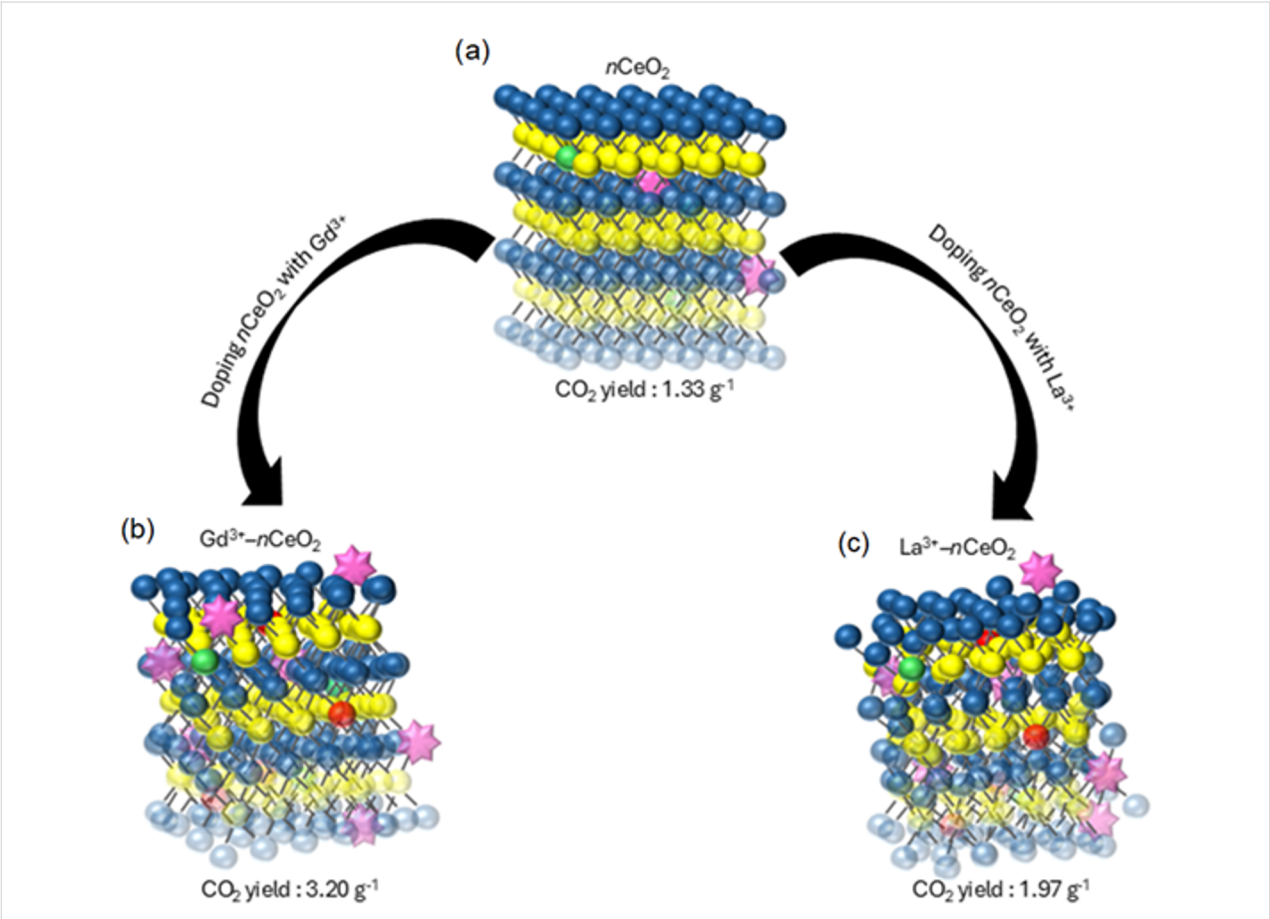

Figure 3: Schematic representation of the proposed defect-related interpretation of CO oxidation over undoped and doped $nCeO_2$ under field-free conditions. The measured CO_2 yields are included for comparison. Oxygen vacancies are indicated by pink stars, while Ce^{4+}, Ce^{3+}, La^{3+}/Gd^{3+} dopants, and oxygen are represented by yellow, green, red, and blue spheres, respectively. The fcc layers are shown with decreasing opacity from the surface to the bulk to visualize the near-surface defect distribution. (a) Undoped $nCeO_2$, showing intrinsic Ce^{3+} formation and associated oxygen vacancies. (b) 5%Gd^{3+}–$nCeO_2$ and (c) 5%La^{3+}–$nCeO_2$, where aliovalent doping increases the oxygen-vacancy population relative to undoped $nCeO_2$. The schematic highlights the higher near-surface vacancy population in 5%Gd^{3+}–$nCeO_2$, consistent with its higher CO_2 yield under field-free conditions. The stronger lattice distortion depicted for 5%La^{3+}–$nCeO_2$ is supported by the XRD analysis.

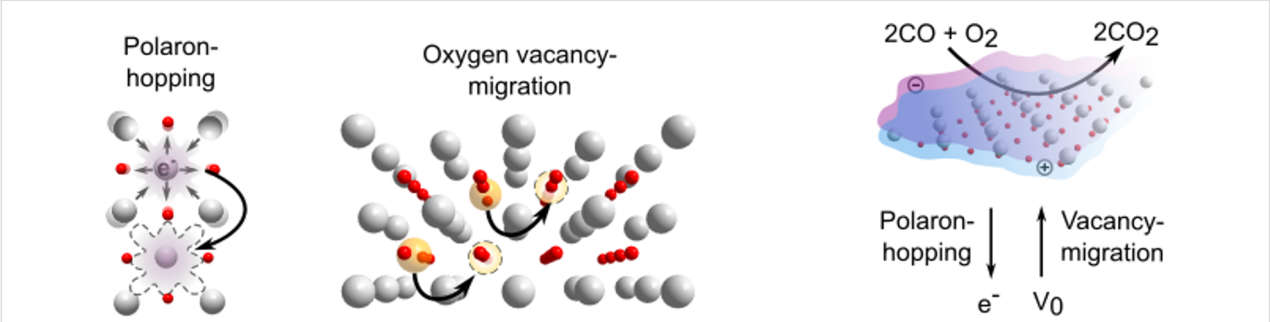

Figure 4: Conceptual schematic representation of possible charge- and defect-transport processes in nCeO$_2$ under an applied electric field. Grey spheres represent Ce^{3+}/Ce^{4+} sites, red spheres represent O^{2-} ions, and yellow spheres indicate V_O. Small-polaron hopping is illustrated as electron transfer between neighbouring Ce^{3+}/Ce^{4+} sites, while V_O migration is shown schematically within the fcc lattice. Under an applied electric field, charge redistribution and defect rearrangement may modify the near-surface defect environment and contribute to the observed field-assisted CO oxidation response. The scheme is intended as a conceptual mechanistic framework rather than direct experimental evidence for quantified polaron or V_O transport in this work.

introduced by Gd^{3+} and La^{3+}. Regarding Ce^{4+} (0.97 Å), Gd^{3+} (1.053 Å) is closer in ionic radius than La^{3+} (1.16 Å); it is therefore expected to perturb the fluorite lattice less strongly. Consistent with this interpretation, the δ values extracted for 5%La^{3+}–nCeO$_2$ from the (111), (200), (220), and (311) reflections are higher than those obtained for nCeO$_2$ and 5%Gd^{3+}–nCeO$_2$ (Figure 5), indicating stronger lattice distortion.

Applying an external potential to bare nCeO$_2$ nearly doubled the apparent CO oxidation efficiency compared with the field-free condition (Figure 6a,b).

The different behaviour of Gd^{3+}- and La^{3+}-doped nCeO$_2$ may also be related to their different interactions with oxygen vacancies. Gd^{3+} incorporation is expected to favour the formation of oxygen vacancies while maintaining a comparatively less distorted fluorite lattice. In contrast, the larger La^{3+} ions can promote the formation of more stable defect associates, such as [La^{3+}-$V_O^{\bullet\bullet}$-La^{3+}] and [La^{3+}-$V_O^{\bullet\bullet}$-Ce^{3+}], which may reduce the ability of oxygen vacancies to rearrange within the lattice or participate in near-surface redox processes [20,36].

Under electrical bias, polarization and charge redistribution at grain surfaces may therefore affect the near-surface Ce^{3+}/Ce^{4+}

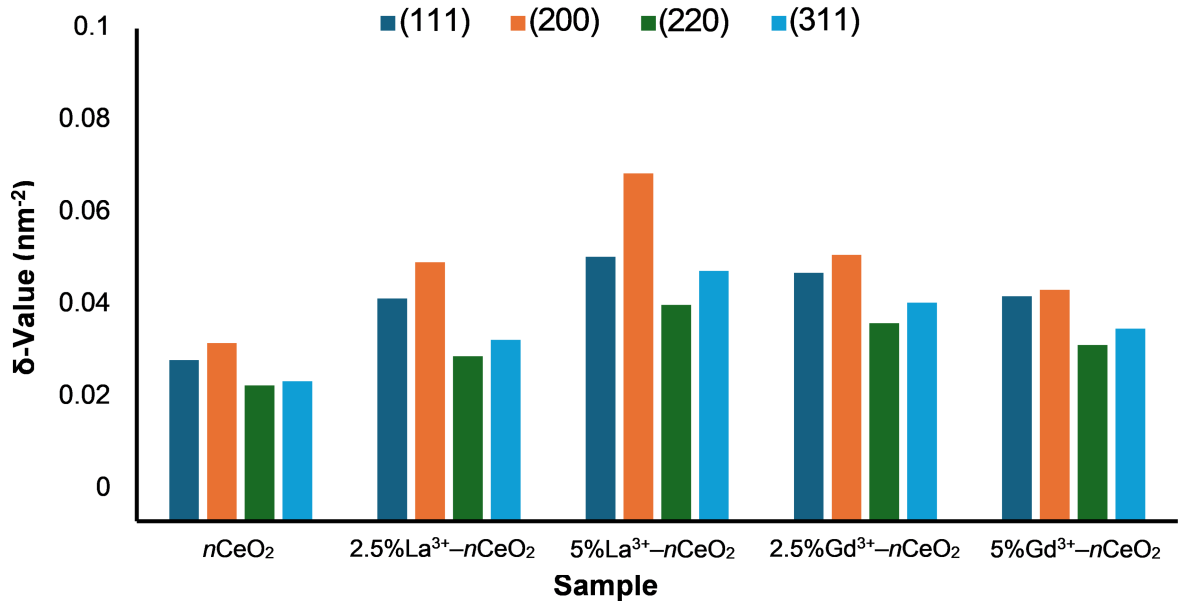

Figure 5: The δ values extracted from the XRD patterns of nCeO$_2$ and doped nCeO$_2$ samples with dopant concentrations of 2.5% and 5%, evaluated from the (111), (200), (220), and (311) reflections. The increase in δ values upon doping indicates enhanced lattice distortion relative to undoped nCeO$_2$, particularly for 5%La^{3+}–nCeO$_2$.

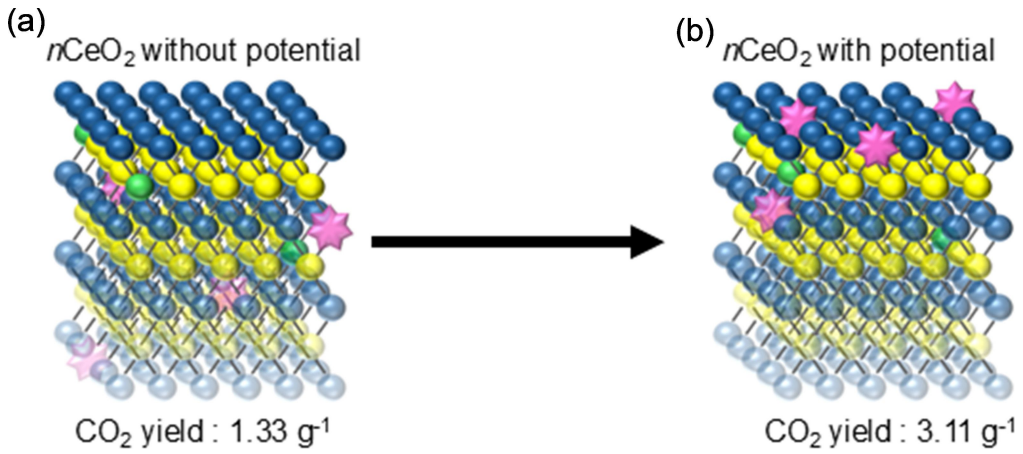

Figure 6: Schematic representation of undoped nCeO$_2$ under field-free conditions and under an applied external potential. Ce^{4+} (yellow), Ce^{3+} (green), O^{2-} (blue), and oxygen vacancies (pink) are represented. The atomic layers are shown with decreasing opacity from the surface to the bulk to suggest depth. (a) nCeO$_2$ under field-free conditions, illustrating a lower near-surface concentration of oxygen vacancies. (b) nCeO$_2$ under an applied potential, schematically illustrating a possible field-induced charge redistribution and a higher near-surface concentration of oxygen vacancies. The measured CO_2 yields are included for comparison. This scheme is intended as a conceptual representation of the field-assisted response and not as direct experimental proof of quantified vacancy transport.

population and the availability of oxygen-vacancy-related defect sites involved in CO oxidation. On this basis, the observed CO oxidation behaviour with and without electrical bias suggests that local changes in oxygen-vacancy distribution and associated Ce^{3+}/Ce^{4+} redox states may modify the near-surface ionic and electronic environment. The pronounced response of nCeO$_2$ and 5%Gd^{3+}–nCeO$_2$ to the applied potential is consistent with possible contributions from small-polaron-related charge transport and oxygen-vacancy rearrangement near the surface. In contrast, the weaker response of 2.5%Gd^{3+}–nCeO$_2$ suggests that the dopant concentration may be insufficient to generate a strong coupled defect/electronic response, while the negligible bias-induced improvement observed for La^{3+}–nCeO$_2$ is consistent with a reduced ability of oxygen vacancies to participate in field-assisted surface redox changes, possibly due to the formation of stable La-associated defect clusters (Figure 7).

We emphasize that this mechanistic interpretation remains descriptive and phenomenological. The present data support a correlation between dopant-dependent defect chemistry, lattice distortion, and bias-assisted CO oxidation behaviour, but they do not directly quantify oxygen-vacancy migration or small-polaron hopping during the reaction. Further systematic studies, such as voltage-dependent measurements, operando spectroscopy, oxygen-isotope exchange, conductivity measurements, or theoretical calculations, would be required to verify the microscopic contributions of these processes. Nevertheless, the present results indicate that applying an electrical bias to reducible oxide catalysts can provide a promising strategy for influencing heterogeneous oxidation reactions, even in the absence of precious metal active phases.

Conclusion

An external electric field can substantially boost room-temperature CO oxidation on nanoscaled ceria by tuning its interfacial defect/redox chemistry. It induces interfacial polarization in ceria based catalysts and boosts CO oxidation under noble-metal-free conditions. The magnitude of the enhancement depends critically on dopant-controlled defect interactions, ion mobility, and electronic polaron transport mechanisms. Undoped nCeO$_2$ shows the largest activity and thus response to the field, with nearly a twofold increase in apparent CO oxidation efficiency under bias, while 5%Gd^{3+}–nCeO$_2$ exhibits a clear synergistic enhancement consistent with sufficient defect mobility and interfacial responsiveness. In contrast, 2.5%Gd^{3+}–nCeO$_2$ appears insufficient for a strong coupled polaron vacancy response, and La^{3+}-doped samples show little to no bias-induced improvement, consistent with stronger defect association/cluster formation that suppresses vacancy participation in sustained field-induced surface redox changes.

Experimental

CO to CO_2 oxidation experiments

The custom-built gas adsorption device consists of sample cell, volume cell, circulation pump, and IR measurement cell, which are interconnected by stainless-steel tubes (6 mm), valves (Swagelok® SS-6P4T-MM-8K), and Swagelok® fittings [37]. The process was conducted under ambient conditions and was controlled by a K-type thermocouple (OMEGA Engineering

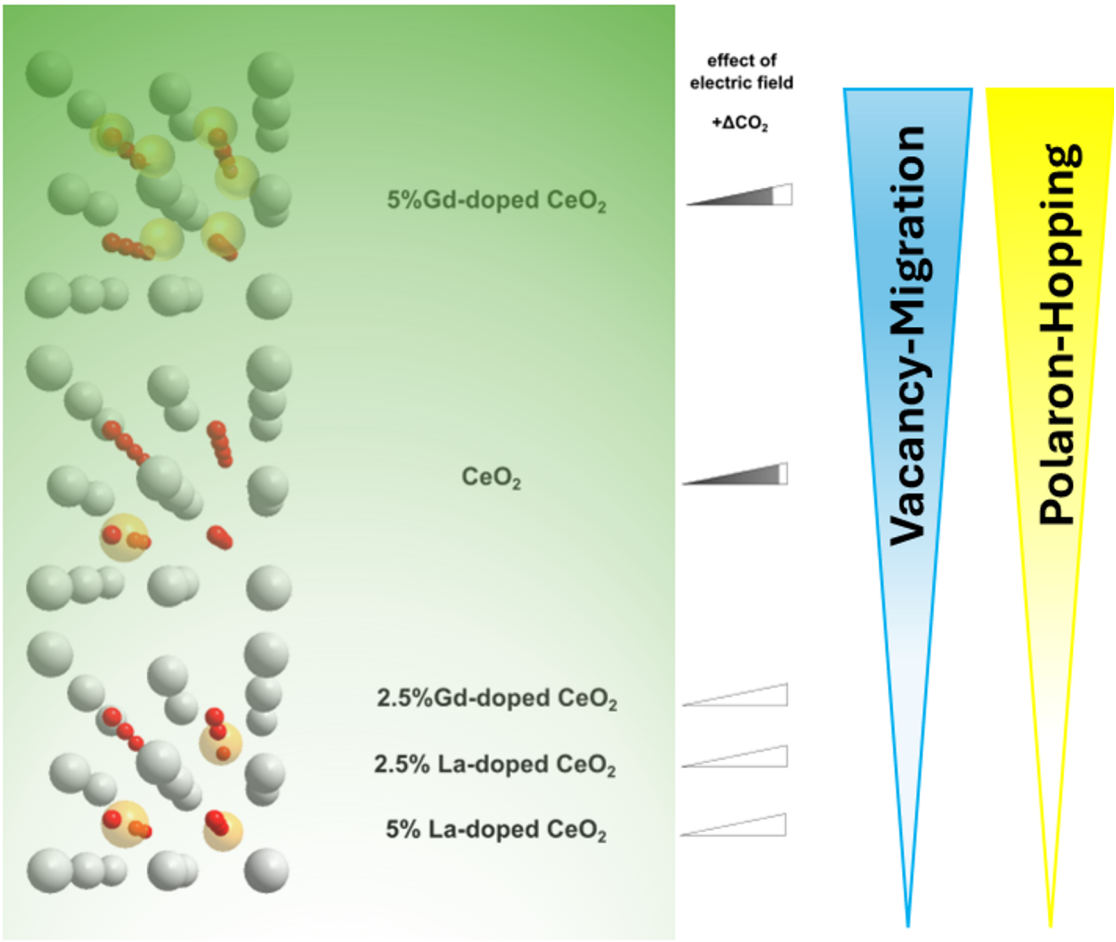

Figure 7: Schematics showing the influence of an external electric field onto $n$$CeO_2$ and differently doped $n$$CeO_2$ samples. The emerging intense green background from top to bottom indicates the increasing combined effect of vacancy migration and polaron hopping onto the performance of the various catalysts. A synergistic effect of polaron hopping and V_O migration is in favour of an enhanced CO oxidation for the low and medium defective samples $n$$CeO_2$ and 5%Gd^{3+}–$n$$CeO_2$. When increasing V_O as in 2.5%Gd^{3+}–$n$$CeO_2$ and 5%La^{3+}–$n$$CeO_2$, the effect of the external applied field is expected to be compensated in the Gd^{3+}-doped samples. La^{3+}-doping however even hinders CO oxidation by V_O cluster formation.

Inc., NiCr, ±1.1 °C) inside the reactor. The outer and inner electrodes of the sample cell were isolated from each other by tubes (PEEK, 6 mm outer diameter, 1.65 mm inner diameter; 3.6 mm outer diameter, and 1.7 mm inner diameter). A Sorensen® XEL 250 DC Power Supply was used to apply the potential to the sample, where the thermocouple inside and the steel mantle of the sample chamber were used as the inner electrode and the outer electrode, respectively. The measurement cell, composed of a steel tube and sealed by two stainless steel caps (0.9 cm window) using PEEK and two Viton® O-rings each, was placed inside a FTIR spectrometer (Thermo Fisher®-Nicolet iS5 with ID1 Transmission Accessory; Software Omnic 9.2.106). Each cap held 1.5 mm thick quartz lenses. The FTIR spectrometer was used to record the gas mixture spectra. A circulation pump (GK-M-12/02) and a pressure transducer (PAA33X-V-30 (0–30 bar), accuracy of 0.05% and resolution of 0.002%) were purchased from Gardner Denver Thomas GmbH, Germany and Omega Newport electronics GmbH, Germany, respectively.

The FTIR spectra were recorded from 400 to 4000 cm^{-1}, considering integration in the ranges from 2143 to 2231 cm^{-1} and from 2283 to 2389 cm^{-1}, related to CO and CO_2 signals, respectively. The integration values for the cell under vacuum and for each measurement were calculated by OMNIC software. The schematic setup of the device is shown in Figure 8.

Oxidation reaction process

The system consisted of three valve-separated compartments, namely, an O_2 chamber (≈17 cm^3), a CO chamber (≈30 cm^3), and a sample chamber (≈18 cm^3). These compartments are indicated by different colours in Figure 8. This configuration allowed the gases to be introduced, isolated, mixed, and

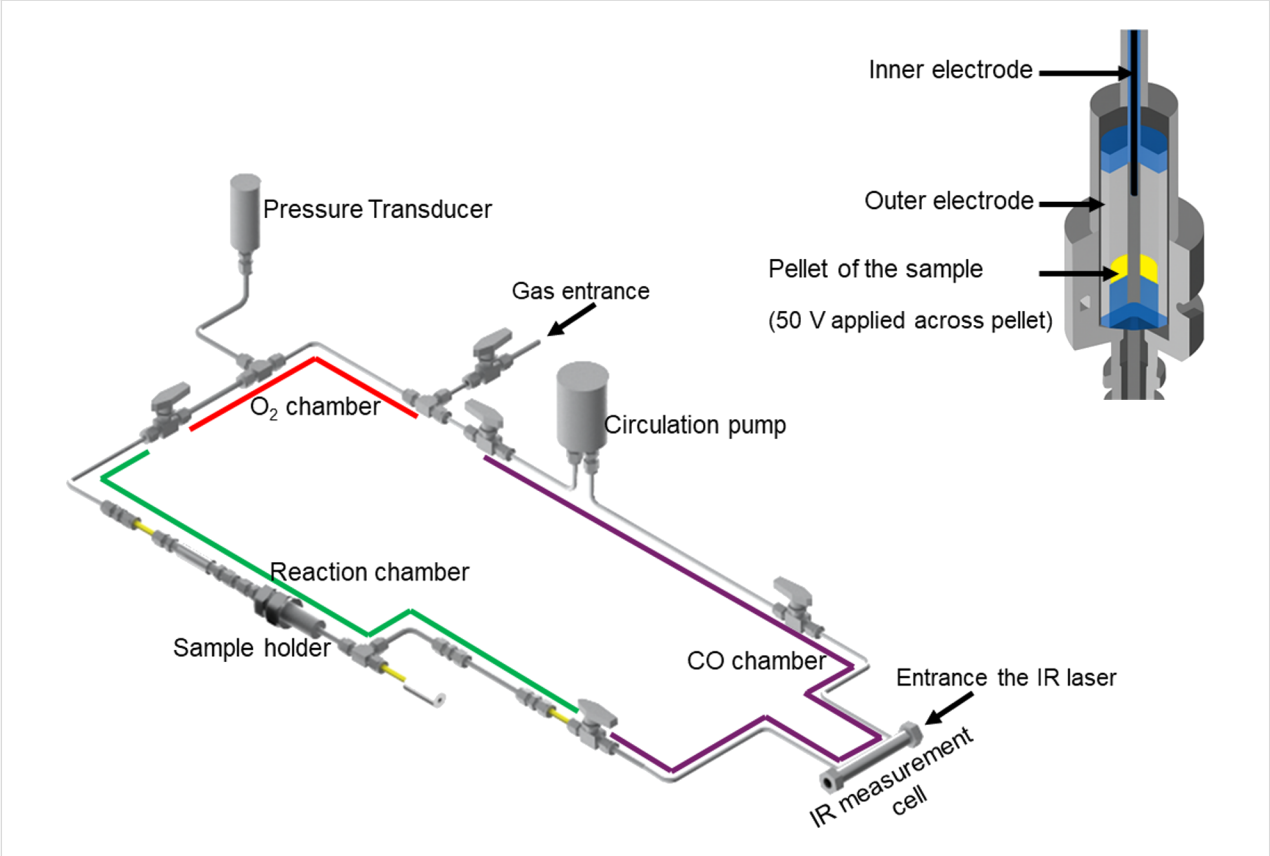

Figure 8: Schematic representation of the gas adsorption/IR measurement setup. The device consists of valve-separated O_2, CO, and sample/reaction chambers, allowing for independent evacuation, gas dosing, equilibration, mixing, and controlled exposure of the catalyst pellet to the gas mixture. The pressure was monitored using a pressure transducer, and CO/O_2 mixing was assisted by a circulation pump. The inset shows the sample-cell configuration, including the inner and outer electrodes and the pressed catalyst pellet. The external voltage was applied across the pressed catalyst pellet through the inner and outer electrodes. The corresponding gas dosing and exposure sequence is summarized in Supporting Information File 1. The graphic was created with Solid Edge. This content is not subject to CC BY 4.0.

exposed to the catalyst in a controlled manner. The pressure in the system was monitored using a pressure transducer, whose output signal was read with a multimeter.

The pressed catalyst pellet was placed in the sample chamber at the end of the cell. The catalyst amounts are shown in Supporting Information File 1, Table S3. Before gas dosing, the sample chamber was heated to approximately 120 °C under vacuum for 15 h to remove weakly adsorbed species, including adsorbed gases, water, and possible residual ammonia, from the sample surface and the cell environment. After this pre-treatment, the system was kept under vacuum and cooled to room temperature before gas dosing. During the vacuum pre-treatment and before gas dosing, the pressure reading was close to zero within the resolution of the pressure-monitoring system. The vacuum spectrum was recorded in this step.

The CO-containing gas mixture, CO/N_2 = 0.1/99.9, Air Liquide, Germany, was first introduced into the CO chamber up to a pressure of 1.5 bar. After an equilibration period of 15 min and reaching a nearly constant pressure signal, the CO chamber (purple region in Figure 8) was isolated by closing the valve between the CO and O_2 chambers. The O_2 chamber was then evacuated for 10 min to remove residual gas before O_2 was introduced up to a pressure of 1.5 bar. The O_2 chamber is shown as the red region in Figure 8. After a further equilibration period of 15 min, the reference CO spectrum was recorded before opening the valve between the CO and O_2 chambers, while the two gases were still kept in separate compartments.

Subsequently, the valve between the CO and O_2 chambers was opened, and the gases were mixed using a circulation pump. After 15 min of mixing/equilibration, the spectrum of the CO/O_2 gas mixture was recorded. The upstream and downstream valves of the sample holder were then opened to expose the catalyst pellet to the gas mixture (the green region in Figure 8). Due to expansion, the pressure of the gas mixture decreased to around 1 bar. Spectra were recorded after 10, 30, 60, 90, and 120 min of contact between the gas mixture and the catalyst.

For the experiments performed under an external electric field, the same gas dosing, mixing, and equilibration procedure was followed. A DC voltage of 50 V was applied using a potentiostat in a two-electrode configuration, with the inner and outer electrodes of the cell serving as the two electrodes. The applied voltage (50 V) generated a DC electric field across the catalyst-containing region. The voltage was applied before opening the upstream and downstream valves of the sample holder and was maintained throughout the full reaction period of 120 min. Spectra were recorded after 10, 30, 60, 90, and 120 min of exposure to the CO/O_2 gas mixture.

The circulation pump was switched off during spectral acquisition. After the final spectrum was collected, the system was evacuated again. A process-flow diagram summarizing the evacuation, gas dosing, equilibration, CO/O_2 mixing, and exposure of the gas mixture to the catalyst pellet is provided in Supporting Information File 1. For details about the calculation of the gas compositions, see Supporting Information File 1.

Supporting Information

Supporting Information File contains more information about synthesis, characterization and raw data values of the measurements.

Supporting Information File 1

Additional information.
[https://www.beilstein-journals.org/bjnano/content/supplementary/2190-4286-17-70-S1.pdf]

Acknowledgements

We appreciate the support of the Ernst-Ruska Center (ERC) Jülich for access to the TEM facilities under contract ERC/TUDa. We thank Dr. Jörg Engstler (TUDa) for performing the measurements. We appreciate the team members of the electrical and mechanical and workshops at TUDa, headed by Matthias Guse and Martin Schwarz for their expert technical support.

Author Contributions

Parastoo Jamshidi: conceptualization; data curation; formal analysis; investigation; methodology; visualization; writing – original draft; writing – review & editing. Silvio Heinschke: conceptualization; formal analysis; investigation; methodology; validation; visualization; writing – original draft; writing – review & editing. Jörg J. Schneider: conceptualization; funding acquisition; methodology; resources; writing – original draft; writing – review & editing.

ORCID® iDs

Jörg J. Schneider - https://orcid.org/0000-0002-8153-9491

Data Availability Statement

All data that supports the findings of this study is available in the published article and/or the supporting information of this article.

References

1. Freund, H.-J.; Meijer, G.; Scheffler, M.; Schlögl, R.; Wolf, M. *Angew. Chem., Int. Ed.* **2011,** *50,* 10064–10094. doi:10.1002/anie.201101378
2. Darade, P. V.; Bhamare, R. G.; Shewale, J. M. *Int. J. Innov. Res. Eng. Multidiscip. Phys. Sci.* **2025,** *13,* 232711.
3. Yan, Y.-Q.; Wu, Y.-Z.; Wu, Y.-H.; Weng, Z.-L.; Liu, S.-J.; Liu, Z.-G.; Lu, K.-Q.; Han, B. *ChemSusChem* **2024,** *17,* e202301778. doi:10.1002/cssc.202301778
4. Abdulwahab, K. O.; Khan, M. M.; Jennings, J. R. *ACS Omega* **2023,** *8,* 30802–30823. doi:10.1021/acsomega.3c01199
5. Kim, S.; Maier, J. *J. Electrochem. Soc.* **2002,** *149,* J73. doi:10.1149/1.1507597
6. Kossoy, A.; Frenkel, A. I.; Wang, Q.; Wachtel, E.; Lubomirsky, I. *Adv. Mater. (Weinheim, Ger.)* **2010,** *22,* 1659–1662. doi:10.1002/adma.200902041
7. Korobko, R.; Lerner, A.; Li, Y.; Wachtel, E.; Frenkel, A. I.; Lubomirsky, I. *Appl. Phys. Lett.* **2015,** *106,* 042904. doi:10.1063/1.4906857
8. Meng, Y.; Liu, S.; Wang, Y.; Xu, W.; Gao, J.; Yu, S.; Su, F.; Zhu, T. *J. Catal.* **2024,** *430,* 115311. doi:10.1016/j.jcat.2024.115311
9. Huan, Y.; Wang, X.; Fang, J.; Li, L. *J. Eur. Ceram. Soc.* **2014,** *34,* 1445–1448. doi:10.1016/j.jeurceramsoc.2013.11.030
10. Devyatov, V. G.; Mikheeva, E. P.; Keier, N. P. *React. Kinet. Catal. Lett.* **1978,** *9,* 199–204. doi:10.1007/bf02068924
11. Oshima, K.; Watanabe, R.; Fukuhara, C.; Kishida, M. *Catal. Lett.* **2024,** *154,* 1398–1403. doi:10.1007/s10562-023-04416-w
12. Grishin, M. V.; Gatin, A. K.; Slutskii, V. G.; Fedotov, A. S.; Kharitonov, V. A.; Shub, B. R. *Russ. J. Phys. Chem. B* **2022,** *16,* 395–398. doi:10.1134/s1990793122030150
13. Grishin, M. V.; Gatin, A. K.; Slutsky, V. G.; Fedotov, A. S.; Kharitonova, V. A.; Shub, B. R. *Russ. J. Phys. Chem. B* **2021,** *15,* 373–376. doi:10.1134/s1990793121020196
14. Grishin, M. V.; Gatin, A. K.; Slutskii, V. G.; Fedotov, A. S.; Kharitonov, V. A.; Shub, B. R. *Russ. J. Phys. Chem. B* **2021,** *15,* 777–781. doi:10.1134/s1990793121050031
15. Grishin, M. V.; Gatin, A. K.; Slutskii, V. G.; Fedotov, A. S.; Kharitonov, V. A.; Shub, B. R. *Russ. J. Phys. Chem. B* **2020,** *14,* 547–551. doi:10.1134/s1990793120030033
16. Grishin, M. V.; Gatin, A. K.; Slutskii, V. G.; Kharitonov, V. A.; Tsyganov, S. A.; Shub, B. R. *Russ. J. Phys. Chem. B* **2016,** *10,* 538–542. doi:10.1134/s1990793116030192
17. Wang, W.; Meng, X.; Wang, Q.; Jiang, X.; Miao, J.; Yao, S.; Wu, Z.; Li, J.; Gao, E.; Zhu, J.; Yao, M.; Dai, Q. *Appl. Catal., B* **2025,** *365,* 124912. doi:10.1016/j.apcatb.2024.124912
18. Hu, Z.; Metiu, H. *J. Phys. Chem. C* **2011,** *115,* 17898–17909. doi:10.1021/jp205432r
19. Nakayama, M.; Martin, M. *Phys. Chem. Chem. Phys.* **2009,** *11,* 3241–3249. doi:10.1039/b900162j

20. Andersson, D. A.; Simak, S. I.; Skorodumova, N. V.; Abrikosov, I. A.; Johansson, B. *Proc. Natl. Acad. Sci. U. S. A.* **2006,** *103,* 3518–3521. doi:10.1073/pnas.0509537103
21. Zhang, L.; Meng, J.; Yao, F.; Zhang, W.; Liu, X.; Meng, J.; Zhang, H. *Inorg. Chem.* **2018,** *57,* 12690–12696. doi:10.1021/acs.inorgchem.8b01853
22. Jayakumar, G.; Albert Irudayaraj, A.; Dhayal Raj, A. *Mech., Mater. Sci. Eng. J.* **2017,** *9,* 127–131.
23. Wu, Z.; Li, M.; Howe, J.; Meyer, H. M., III; Overbury, S. H. *Langmuir* **2010,** *26,* 16595–16606. doi:10.1021/la101723w
24. Banerji, A.; Grover, V.; Sathe, V.; Deb, S. K.; Tyagi, A. K. *Solid State Commun.* **2009,** *149,* 1689–1692. doi:10.1016/j.ssc.2009.06.045
25. Metiu, H.; Chrétien, S.; Hu, Z.; Li, B.; Sun, X. *J. Phys. Chem. C* **2012,** *116,* 10439–10450. doi:10.1021/jp301341t
26. Hernández, W. Y.; Laguna, O. H.; Centeno, M. A.; Odriozola, J. A. *J. Solid State Chem.* **2011,** *184,* 3014–3020. doi:10.1016/j.jssc.2011.09.018
27. Ni, C.; Wang, K.; Jin, L.; Liu, Y.; Chen, J.; Yang, L.; Ji, C.; Xu, H.; Li, Z.; Tian, L. *Chem. Commun.* **2025,** *61,* 658–668. doi:10.1039/d4cc04740k
28. Tsuchiya, T.; Miyoshi, S.; Yamashita, Y.; Yoshikawa, H.; Terabe, K.; Kobayashi, K.; Yamaguchi, S. *Sci. Technol. Adv. Mater.* **2013,** *14,* 045001. doi:10.1088/1468-6996/14/4/045001
29. Zhang, D.; Han, Z.-K.; Murgida, G. E.; Ganduglia-Pirovano, M. V.; Gao, Y. *Phys. Rev. Lett.* **2019,** *122,* 096101. doi:10.1103/physrevlett.122.096101
30. Wu, H.; Abdi, F. F.; Ng, Y. H. *Angew. Chem., Int. Ed.* **2026,** *65,* e22726. doi:10.1002/anie.202522726
31. Franchini, C.; Reticcioli, M.; Setvin, M.; Diebold, U. *Nat. Rev. Mater.* **2021,** *6,* 560–586. doi:10.1038/s41578-021-00289-w
32. Jiang, X.; Cheng, X.; Liu, Z.; Ding, L.; Han, W. *Phys. Chem. Chem. Phys.* **2025,** *27,* 21673–21682. doi:10.1039/d5cp02631h
33. Su, Y.-Q.; Filot, I. A. W.; Liu, J.-X.; Tranca, I.; Hensen, E. J. M. *Chem. Mater.* **2016,** *28,* 5652–5658. doi:10.1021/acs.chemmater.6b01548
34. Larsen, D. M. *Phys. Rev.* **1964,** *133,* A860–A866. doi:10.1103/physrev.133.a860
35. Han, Z.-K.; Liu, W.; Gao, Y. *JACS Au* **2025,** *5,* 1549–1569. doi:10.1021/jacsau.5c00095
36. Li, S.; Lu, X.; Shi, S.; Chen, L.; Wang, Z.; Zhao, Y. *Front. Chem. (Lausanne, Switz.)* **2020,** *8,* 348. doi:10.3389/fchem.2020.00348
37. Heinschke, S.; Schneider, J. J. *Adv. Sci.* **2025,** *12,* e04617. doi:10.1002/advs.202504617

License and Terms